JOURNAL OF GEOPHYSICAL RESEARCH, VOL. 112, C09020, doi:10.1029/2007JC004205, 2007

Langmuir turbulence and deeply penetrating jets in an unstratified mixed layer

Jeff A. Polton[1] and Stephen E. Belcher[2]

Received 8 March 2007; revised 4 June 2007; accepted 18 June 2007; published 25 September 2007.

[1] The influence of surface waves and an applied wind stress is studied in an ensemble of large eddy simulations to investigate the nature of deeply penetrating jets into an unstratified mixed layer. The influence of a steady monochromatic surface wave propagating parallel to the wind direction is parameterized using the wave-filtered Craik-Leibovich equations. Tracer trajectories and instantaneous downwelling velocities reveal classic counterrotating Langmuir rolls. The associated downwelling jets penetrate to depths in excess of the wave's Stokes depth scale, δ_s. Qualitative evidence suggests the depth of the jets is controlled by the Ekman depth scale. Analysis of turbulent kinetic energy (tke) budgets reveals a dynamical distinction between Langmuir turbulence and shear-driven turbulence. In the former, tke production is dominated by Stokes shear and a vertical flux term transports tke to a depth where it is dissipated. In the latter, tke production is from the mean shear and is locally balanced by dissipation. We define the turbulent Langmuir number $La_t = (v_*/U_s)^{0.5}$ (v_* is the ocean's friction velocity and U_s is the surface Stokes drift velocity) and a turbulent anisotropy coefficient $R_t = \overline{w'^2}/(\overline{u'^2} + \overline{v'^2})$. The transition between shear-driven and Langmuir turbulence is investigated by varying external wave parameters δ_s and La_t and by diagnosing R_t and the Eulerian mean and Stokes shears. When either La_t or δ_s are sufficiently small the Stokes shear dominates the mean shear and the flow is preconditioned to Langmuir turbulence and the associated deeply penetrating jets.

Citation: Polton, J. A., and S. E. Belcher (2007), Langmuir turbulence and deeply penetrating jets in an unstratified mixed layer, *J. Geophys. Res.*, *112*, C09020, doi:10.1029/2007JC004205.

1. Introduction

[2] Waves are a ubiquitous feature of the surface ocean that combined with even a light surface wind stress can produce upper ocean quasi two-dimensional instabilities known as Langmuir circulations. These features were reported by *Langmuir* [1938] following an Atlantic crossing where he observed Sargassum weed arranging into linear bands aligned with the wind direction. These flotsam streaks are the surface signature of counter rotating Langmuir circulation vortices. These features have been observed to penetrate deeply [*Pollard and Thomas*, 1989] and subsequent observational campaigns have led to the documentation of their structure and variability [e.g., *Plueddemann et al.*, 1996]. It is widely accepted that the Langmuir circulations are generated through an instability which arises through an interaction between the Stokes drift of the waves and the local vorticity. The effect can be incorporated into the Navier-Stokes equations by a process called wave filtering, giving rise to the wave-filtered equations [*Craik and Leibovich*, 1976].

[1]Scripps Institution of Oceanography, University of California, San Diego, La Jolla, California, USA.
[2]Department of Meteorology, University of Reading, Reading, UK.

0148-0227/07/2007JC004205$09.00

[3] Large eddy simulation (LES) of these equations was pioneered by *Skyllingstad and Denbo* [1995] and *McWilliams et al.* [1997]. More recent contributions have further developed the field addressing higher complexity problems, for example notable studies include effects of wave breaking [*Noh et al.*, 2004; *Sullivan et al.*, 2004] (see also P. P. Sullivan et al., Surface gravity wave effects in the oceanic boundary layer: Large-eddy simulation with vortex force and stochastic breakers, submitted to *Journal of Fluid Mechanics*, 2007), buoyancy forcing [*Li et al.*, 2005], biology [*Lewis*, 2005] and a modified K-profile parameterization [*Smyth et al.*, 2002]. For a comprehensive review on Langmuir circulations, refer to *Thorpe* [2004]. In particular, *Sullivan et al.* [2004] describe a downward turbulent kinetic energy flux that is a product of a stochastic parameterization for the effect of wave breaking at the surface. However, a similar transport effect can also be seen without wave breaking, that is in less extreme weather conditions. *McWilliams et al.* [1997] demonstrate evidence of enhanced downwelling in their simulations without recourse to wave breaking parameterizations. We investigate how this process varies with the external wave parameters. Additionally of particular interest to this study, *Li et al.* [2005] vary the size of the surface Stokes drift and use the relative magnitudes of depth averaged velocity variances to classify turbulence regimes in wave forced simulations of the ocean mixed layer. They demonstrate, for strong enough Stokes drift, a transition

occurs in the nature of the mixed layer turbulence from a shear-driven turbulence to a Langmuir turbulence. By retaining depth-dependent information in our diagnostics, we investigate further how this transition varies as a function of the wave forcing depth scale.

[4] Non parallel wind and wave forcing [*Gnanadesikan and Weller*, 1995; *Polonichko*, 1997]; density structure [*Li and Garrett*, 1997] and time-dependent forcing [*Skyllingstad et al.*, 2000] will doubtless have an effect on the surface layer dynamics as modeled in eddy viscosity models, however since much less is known about the influence of the wave forcing in a fully 3D turbulent flow this study's objective is to investigate as clean an experiment as usefully possible. There still much to be gained by investigating the simplest LES scenarios to highlight clearly the role of the wave induced processes. We consider the case with a constant density, steady wind forcing, and monochromatic wave forcing (as parameterized through the Craik-Leibovich equations) that is in a direction parallel to the wind. Parallel and steady wind and wave forcing are chosen for this study of Langmuir turbulence since this configuration has the fastest growing linear instabilities [*Polonichko*, 1997]. This investigation is into the nature of the vertical structure of a mixed layer where wave induced downwelling jets are capable of being the principle transport mechanism [*Gnanadesikan and Weller*, 1995]. To this end we analyze data from an ensemble of LES runs to investigate how the wave parameters control the statistically steady state dynamics of the mixed layer.

[5] In section 2 the LES model formulation and parameter ranges are presented. In section 3 the complex three dimensional structure of the flow field is dissected using trajectories, instantaneous velocity sections and turbulent kinetic energy budgets. These analyses motivate diagnostics, presented in section 4, that compare Stokes shear to mean shear and that quantify anisotropy in the turbulence in order to describe the vertical structure of the Langmuir turbulence. We conclude with a discussion in Section 5.

2. LES Model and Simulations

2.1. Model Formulation

[6] Turbulent motions in the mixed layer are represented using large eddy simulations (hereafter LES), where the fully nonlinear equations of motion are integrated forward in time with sufficient resolution to compute explicitly the large-scale turbulent motions. Previous computational studies of turbulent Ekman layers include those by *Coleman* [1999] and *Zikanov et al.* [2003]. Here we are also interested in the effect of surface waves, which are parameterized using the deep water expression for Stokes drift velocity,

$$u_s = U_s e^{(z/\delta_s)} \tag{1}$$

where $\delta_s = 1/2k$ is the Stokes depth scale for a monochromatic surface wave with wave number k [*Phillips*, 1977].

[7] Following *Skyllingstad and Denbo* [1995] and *McWilliams et al.* [1997], we perform LES of the wave filtered Craik-Leibovich (C-L) equations to account for wave-length averaged effects of surface waves. These equations are

$$\frac{D\boldsymbol{u}}{Dt} + \boldsymbol{f} \times (\boldsymbol{u} + \boldsymbol{u}_s) = -\nabla\pi - \frac{g\rho'}{\rho_0}\hat{\mathbf{z}} + \boldsymbol{u}_s \times \boldsymbol{\omega} + SGS, \tag{2}$$

$$\nabla \cdot \boldsymbol{u} = 0, \tag{3}$$

$$\frac{D\theta}{Dt} + \boldsymbol{u}_s \cdot \nabla\theta = SGS. \tag{4}$$

Here $\boldsymbol{u} = (u, v, w)$ is the three-dimensional wave-averaged Eulerian velocity, $\boldsymbol{f} = f\hat{\mathbf{z}}$ is the Coriolis parameter, $\hat{\mathbf{z}}$ is the upward unit vector, $\boldsymbol{\omega} = \nabla \times \boldsymbol{u}$ is the local vorticity vector, the equation of state is a simple function of temperature such that $-\frac{\rho'}{\rho_0} = \frac{\theta'}{\theta_0}$ for $\theta_0 = 288.17K$ and $\rho_0 = 1000\ kg\ m^{-3}$, and $D/Dt = \partial/\partial t + \boldsymbol{u} \cdot \nabla$ is the material derivative. The subgrid-scale processes (denoted *SGS*) are parameterized using a first-order Smagorinsky closure model and also include molecular viscosity and diffusion terms that are kept for numerical stability purposes. Finally, π is the generalized pressure given by

$$\pi = \frac{p}{\rho_0} + \frac{1}{2}\boldsymbol{u}_s^2 + \boldsymbol{u} \cdot \boldsymbol{u}_s. \tag{5}$$

Whilst one could redefine pressure to be π [*Noh et al.*, 2004], formal derivations of the wave filtered equations [see, e.g., *Holm*, 1996] give rise to the $\boldsymbol{u} \cdot \boldsymbol{u_s}$ dynamic pressure. Explicitly separating this term from pressure results in a more natural partition of fluxes in the turbulent kinetic energy budget.

[8] The equations are integrated numerically using a code based on the UK Met Office atmospheric boundary layer code BLASIUS [*Wood and Mason*, 1993], which has been modified to include the two wave forcing terms. The code is run in LES mode [*Brown et al.*, 2001] using a Smagorinsky subgrid model. For further model details refer to *Wood et al.* [1998], *Lewis* [2005] and *Polton et al.* [2005]. The domain is periodic and isotropic in the horizontal directions spanning 120 m with a resolution of 3 m. In the vertical direction 200 grid points span 90 m with a resolution of 0.46 m. This is similar to the 3 m × 3 m × 0.6 m resolution used by *McWilliams et al.* [1997], which is vertically uniform. Our simulations also have uniform vertical resolution except in the upper 1 m where we use a stretched grid over 4 levels. At the surface a constant wind stress, $\tau = 0.037$ N m^{-2} (corresponding to a wind speed of about 5 m s^{-1}), is applied in the x direction. This is expressed as a boundary condition on the horizontal shear at a depth of the surface roughness length, $z = -z_0$, below the surface,

$$\kappa_m \frac{\partial u}{\partial z} = v_*^2 = \frac{\tau}{\rho_0}; \qquad \kappa_m \frac{\partial v}{\partial z} = 0, \tag{6}$$

where κ_m is the mixing-length eddy viscosity, which is determined by the subgrid-scale *Smagorinsky* [1963] closure model, and v_* is the friction velocity. At the surface

Table 1. Simulation Parameters[a]

Run Number	U_s, m s^{-1}	k, m^{-1}	f, $\times\ 10^{-4}$ s^{-1}	La_t	δ_s, m
R0	0.068	0.105	1.0	0.2995	4.7619
R1	0.017	0.02625	1.0	0.5990	19.0476
R2	0.034	0.02625	1.0	0.4236	19.0476
R3	0.068	0.02625	1.0	0.2995	19.0476
R4	0.271	0.02625	1.0	0.1500	19.0476
R5	0.017	0.0525	1.0	0.5990	9.5238
R6	0.034	0.0525	1.0	0.4236	9.5238
R7	0.068	0.0525	1.0	0.2995	9.5238
R8	0.271	0.0525	1.0	0.1500	9.5238
R9	0.017	0.105	1.0	0.5990	4.7619
R10	0.034	0.105	1.0	0.4236	4.7619
R11	0.068	0.105	1.0	0.2995	4.7619
R12	0.271	0.105	1.0	0.1500	4.7619
R13	0.017	0.21	1.0	0.5990	2.3810
R14	0.034	0.21	1.0	0.4236	2.3810
R15	0.068	0.21	1.0	0.2995	2.3810
R16	0.271	0.21	1.0	0.1500	2.3810
R17	0.068	0.105	0.0	0.2995	4.7619
R18	0.068	0.105	0.5	0.2995	4.7619
R19	0.068	0.105	1.5	0.2995	4.7619
R20	0.0	0.0	1.0	∞	∞

[a]R0 is the control simulation and for convenience is also relabeled R11.

a small cooling buoyancy flux of 5 W m^{-2} is applied to initiate vertical motion. This gives the same surface Monin-Obukhov length scale, $L_{mon} = -240$ m, as set by *McWilliams et al.* [1997] and *Lewis* [2005] and since this is much greater than the domain depth the dynamics are dominated by shear rather than convective processes.

[9] The subgrid-scale *Smagorinsky* [1963] scheme is employed to represent the unresolved Reynolds stresses using the strain tensor, S_{ij},

$$(\text{SGS Reynolds stress})_{ij} = -\kappa_m S_{ij} = -\kappa_m \left(\frac{\partial u_i}{\partial x_j} + \frac{\partial u_j}{\partial x_i} \right), \quad (7)$$

where the eddy viscosity, κ_m, is determined from the strain tensor squared and a new mixing length, L_m, such that

$$\kappa_m = L_m^2 \sqrt{\frac{S_{ij}S_{ij}}{2}\left(1 - Ri_f\right)}. \quad (8)$$

There are two things to note here. Firstly the Richardson flux, Ri_f, number dependence accommodates the role of buoyancy forcing away from the surface [*Mason and Sykes*, 1982]. Secondly, we choose L_m to simulate a log layer velocity solution very near the surface and then to be a constant, $L_0 = 1$ m, away from the surface. Other LES use a dynamic Smagorinsky parameterization [e.g., *Zikanov et al.*, 2003] that calculates L_m as a function of the local velocity. However solutions with this approach, though better in the interior, do not smoothly match an applied stress surface boundary condition. Therefore, following *Blackadar* [1962] and *Mason and Sykes* [1982], we use

$$\frac{1}{L_m^2} = \left(\frac{\phi_m \left(1 - Ri_f\right)^{0.25}}{\kappa(z + z_0)} \right)^2 + \frac{1}{L_0^2}, \quad (9)$$

where ϕ_m is the Monin-Obukhov similarity function defined such that $\partial u/\partial z = v_* \phi_m\ ([z + z_0]/L_{mon})/[\kappa(z + z_0)]$, for κ = 0.4 and roughness length z_0.

[10] No attempt is made to represent mixing by breaking waves. At the lower boundary, $z = -90$ m, a no-slip condition is imposed (although the domain was sufficiently deep that this boundary condition did not play a dynamical role).

[11] The most significant difference between our simulations and those of *McWilliams et al.* [1997] is in the stratification. In their study, only the upper 33 m has a constant reference density, ρ_0, which sits on a weakly stratified interior fluid with uniform buoyancy frequency. We choose to simplify the dynamics by making the reference density for the whole domain a constant in order to isolate clearly the effects of the wave processes from any imposed depth scales.

[12] The code was checked by performing a simulation with the parameters of *McWilliams et al.* [1997]. Vertical profiles of the mean flow and turbulence statistics from our simulation (Figure 5 in section 4) are in good agreement with *McWilliams et al.* [1997].

2.2. Model Run Details

[13] A number of simulations are performed for a range of parameters: varying the Coriolis parameter, f, and the wave parameters U_s and k. Each of the simulations has $v_* = 6.1 \times 10$ ms^{-1}(corresponding to a 10 m atmospheric wind speed, $U_{10} \approx 5$ ms^{-1}. The roughness of the sea surface from below is taken to be z_0 = 0.1 m, which is smaller than the values used by *Craig and Banner* [1994], but experience with the linear eddy viscosity model [*Polton et al.*, 2005] indicates that the current profiles in the bulk of the Ekman layer are insensitive to this parameter. The simulations are given in Table 1. The wave parameters are k = 0.02625, 0.0525, 0.105, 0.210 m^{-1}, which yield wavelengths λ = 240, 120, 60, 30 m, and the surface Stokes drift coefficients are U_s = 0, 0.017, 0.034, 0.068, 0.271 ms^{-1}. Simulation R0 is the *McWilliams et al.* [1997] control run and is identical to R11.

[14] *Lewis and Belcher* [2004] show that, with a constant viscosity, the transient motions, with and without Coriolis-Stokes forcing, decay on the inertial period $T = O(2\pi/f) \approx 6 \times 10^4$ s. Hence each run was integrated to 2×10^5 s $- 4 \times 10^5$ s, which is at least three inertial periods. Profiles of the second-order turbulence moments were monitored and satisfactory steady state was seen after this time. Mean flow and turbulent statistics were gathered starting at 5000 s and computed from instantaneous horizontal averages that are taken approximately every 10 s.

[15] In this numerical model setup there are only four external controlling parameters (that is, once a statistically steady state is reached). These are the friction velocity, v_*, the magnitude of the surface Stokes drift, U_s, the Coriolis parameter, f, and the wave number of the parameterized surface wave forcing, k. By resolving the eddies we remove the dependence on eddy viscosity and include f as a dependent variable via the Ekman depth scale, $\delta_e = v_*/f$. Hence there are three important parameters that control the model's solutions: the Ekman scale δ_e, the Stokes depth scale δ_s, and the turbulent Langmuir number, $La_t = (v_*/U_s)^{0.5}$.

3. A Dynamical Exploration of the Model

[16] In the following section we present a portrait of the LES dynamics by considering a number of diagnostic

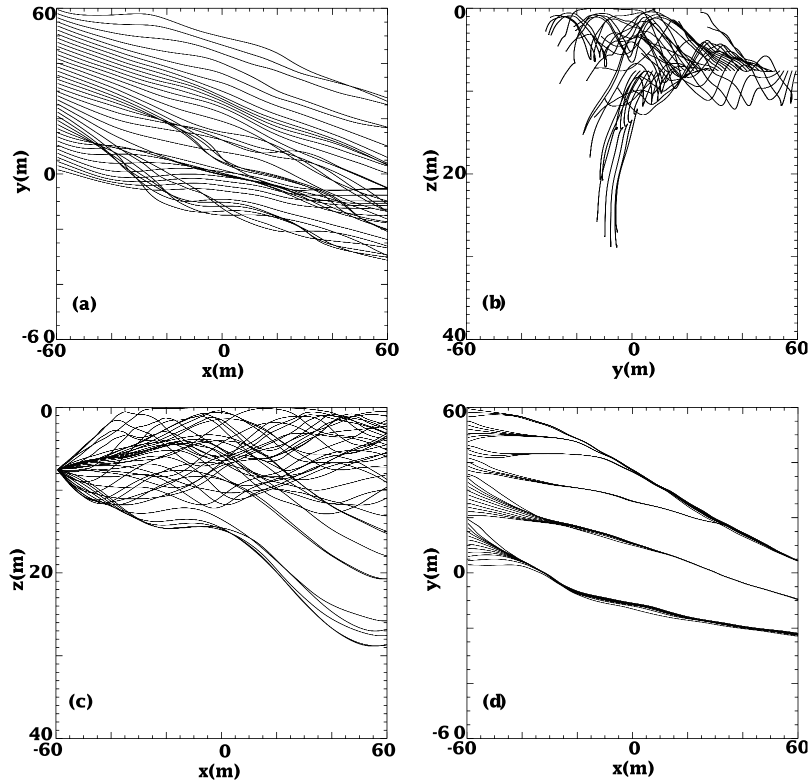

Figure 1. Parcels advected by near-surface turbulence in simulation R0. (a–c) Parcels released along a line of constant depth (7.5m) and x. (d) Surface trapped parcels released along a line of constant x. The wind and waves move in the positive x direction.

approaches. In order to facilitate comparison with established literature we describe the trajectory and vertical velocity diagnostics using the control simulation R0. Then we consider turbulent kinetic energy budgets in 4 simulations, varying the controlling parameters.

3.1. Particle Trajectories

[17] Passive tracers are released and tracked in the model domain to investigate the Lagrangian pathways. Figure 1 shows particles released in the statistically steady control simulation R0 (after an integration of 6 inertial oscillation periods) and tracked until they leave the domain (approximately one hour for the deeply penetrating, slower, particles). Figures 1a–1c show particles released along a line perpendicular to the wind and waves and at a constant depth. Figure 1a shows that the dominant flow is a mean drift to the southeast. Figure 1b shows that downward flux events are more intense and less frequent than the upward events, consistent with a zero net vertical mass flux. Together the along and across stream depth sections, Figures 1b and 1c, show that there are helical motions on top of the mean drift, confirming that the wave-filtered equations are able to represent roll motions consistent with the classical Langmuir circulation picture. Figure 1d shows trajectories for a set surface trapped particles and can be compared with observational data [*Plueddemann et al.*, 1996] and the trajectories shown by *McWilliams et al.* [1997]. Notice that only the surface trapped particles converge and that the length scale between the streaks is set by the duration of the forcing, not by the scale of the Langmuir circulations. As time progresses, convergence and divergence lines appear and disappear. Existing lines are split only if they span a divergence line, but two lines converge if they are brought close enough together to be within one convergence region. If particles were released from all positions on the surface then the streaks would form in the streamwise direction and the whole pattern would drift to the south east with the mean flow. Therefore we see the Langmuir circulations as vortices in the streamwise direction imposed on the mean flow that drifts southeast at the surface with spacing between streaks determined by the forcing duration.

3.2. Instantaneous Vertical Velocity

[18] Figure 2 show instantaneous contour plots of horizontal sections of w for increasing depth in simulation R0. The shading denotes upwelling (black) and downwelling (white). Near the surface the presence of fine-scale structures aligned with the wind is consistent with observations of Langmuir circulations. The intensity of the downwelling events are measured by the fractional area of downwelling (after the *Leibovich* [1983] 3rd criterion for Langmuir rolls which states that the regions of downwelling must be more intense than the upwelling regions for Langmuir circulations). In Figure 2 the scale of the downwelling intensity is shown to increase to a depth of 2 δ_s to 3 δ_s, but that it is a flat function of depth down to 4 δ_s, at which depth the coherency of the downwelling region breaks down. Note also that the downwelling streaks align more closely to the surface mean current than to the current at any particular

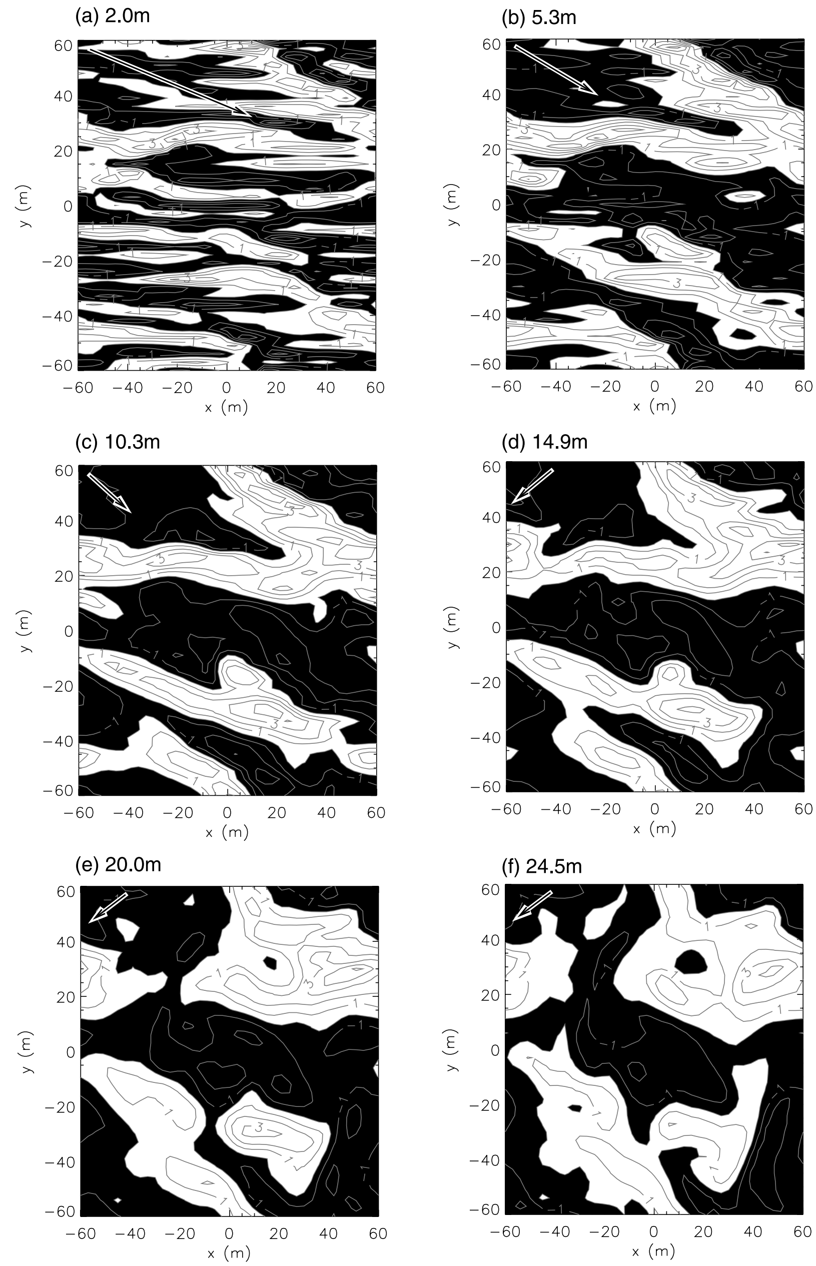

Figure 2. Instantaneous w contours, illustrating the presence of horizontally aligned vortex tubes in simulation R0. The white shading denotes downwelling. The depth as a multiple of the Stokes depth and the percentage area of downwelling is given for each plot: (a) $0.4\delta_s$, 48%, (b) δ_s, 43%, (c) $2\delta_s$, 40%, (d) $3\delta_s$, 39%, (e) $4\delta_s$, 41%, and (f) $5\delta_s$, 45%. The contour interval is v_*. In each plot the vector denotes the total mean Lagrangian velocity for that depth. Their magnitudes as multiples of v_* are: 6.24, 3.24, 1.86, 1.64, 1.46, 1.26.

depth (shown as the arrow in Figure 2) supporting the claim that these are surface forced features.

[19] Thus wave effects penetrate much deeper than the Stokes drift via coherent near surface downwelling zones. This is consistent with the trajectory perspective: occasionally a strong downwelling jet will penetrate to depths much greater than the Stokes depth scale. However, what controls the depth of penetration that is in excess of the Stokes depth scale? By varying the Ekman depth δ_e, via f, there is qualitative evidence that the depth scale of the jets also varies. Figure 3 shows four representative snapshots of across-wind depth profiles of the vertical velocity field taken from animations of 4 simulations (R17, R18, R0, R19) varying $f = (0, 0.5, 1, 1.5) \times 10^{-4}$ s^{-1}. For each of these runs the Stokes depth ($\delta_s = 5.3$ m) is much less that the Ekman depth scale. Each run is integrated to at least $20 \times H/v_*$, a proxy for the eddy turnover time. Though this is only 2.4 inertial periods for simulation R18 (with smallest $f \neq 0$) the presence of Langmuir cells is known to more vigorously mix fluid than by viscous stresses alone [see, e.g., *Gargett et al.*, 2004]. On each of these representative snapshots a dashed line is drawn to mark the maximum depth of the

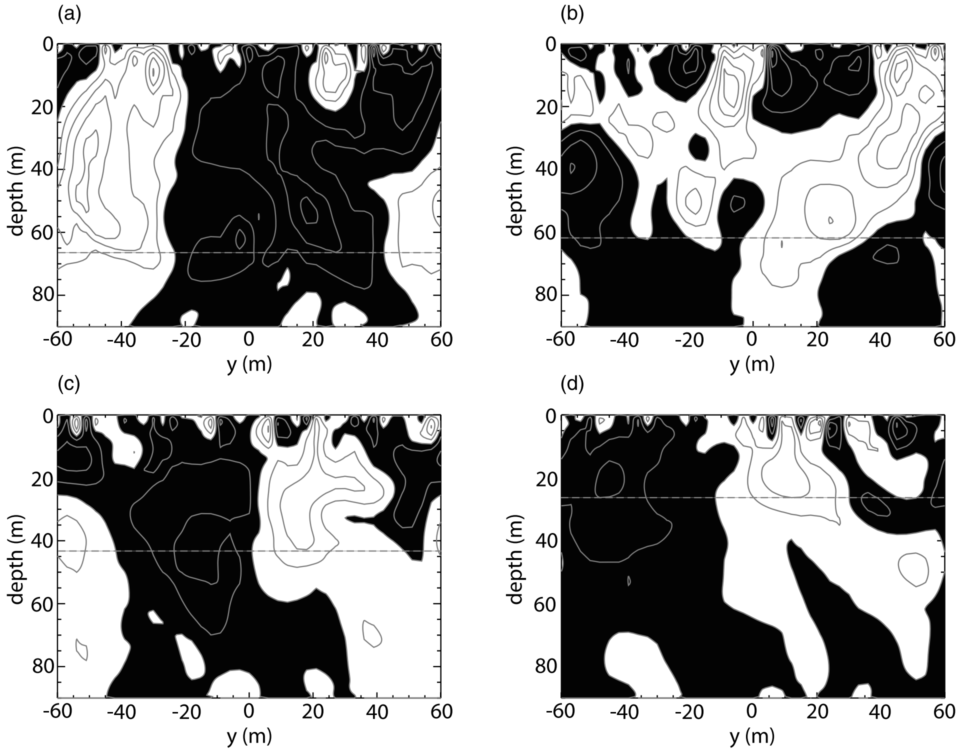

Figure 3. Depth cross sections of vertical velocity to show the jet structure when varying *f*. (a) R17: $\delta_e = \infty$. (b) R18: $\delta_e = 122$ m. (c) R0: $\delta_e = 61$ m. (d) R19: $\delta_e = 41$ m. White is downwelling. Contour interval is v_*. The dashed line marks the deepest occurrence of $w = 2v_*$ as an ad hoc proxy for depth of jets. Penetration depth decreases with decreasing δ_e.

$w = 2v_*$ contour demonstrating qualitatively that the depth of jet penetration increases with δ_e.

[20] Thus we see the vertical extent of enhanced mixing of momentum by the Langmuir jets is constrained by the Ekman depth scale. Assuming that deeper penetrating turbulence can be associated with more energetic turbulence then an interesting comparison can be made with findings of *Skyllingstad et al.* [2000]. These authors report that the turbulent strength increases when the wind and wave forcing is allowed to rotate with the interial currents. This scenario is equivalent to setting the Coriolis parameter to zero, imposing fixed wind and wave forcing and neglecting the Stokes-Coriolis force [*Skyllingstad et al.*, 2000], consistent with our finding that the penetration depth increases with the Ekman depth scale under steady wind and wave forcing.

3.3. Turbulent Kinetic Energy Budgets

[21] We have seen in the previous section that the wave forcing produces Langmuir rolls in the Stokes layer and that these give rise to jets that penetrate much deeper. We investigate these jets using turbulent kinetic energy (hereafter tke) budgets. In the following, prime terms denote deviations from the statistically steady horizontal mean (bar) terms, turbulent kinetic energy is defined as $e = \overline{(u'^2 + v'^2 + w'^2)}/2$ and ε is the subgrid-scale dissipation. Then the statistically steady tke equation for (2) is given by

$$\overline{u'w} \cdot \frac{\partial \overline{\boldsymbol{u}}}{\partial z} + \overline{u'w}\frac{\partial u_s}{\partial z} + \frac{\partial \overline{e'w}}{\partial z} + \frac{1}{\rho_0}\frac{\partial \overline{p'w}}{\partial z} - \frac{g}{\theta_0}\overline{\theta' w} = \epsilon. \qquad (10)$$

In this section we investigate the effect of varying wave parameters, on the tke budgets, to discover the physical mechanisms that govern the turbulent dynamics.

[22] On the left hand side of (10) there are two shear production terms of tke. The 1st term represents the extraction of tke from the mean flow by the eddies and is referred to as the mean shear production term. The second term represents the extraction of tke from the Stokes flow and is referred to as the Stokes shear production term. The next two terms are transport terms; transport of the tke anomalies by correlated vertical velocity anomalies and pressure anomalies. Lastly on the left hand side is the production of tke by diabatic processes. This is negligible in our isothermal simulations.

[23] Figure 4 shows the turbulent kinetic energy budget profiles for selected simulations. Figure 4a is the control run, R0. Figure 4b, R9, has a doubled La_t relative to the control run. Figure 4c, R15, has a doubled k relative to the control run. Figure 4d, R20, is a pure shear simulation. In each plot the component terms in the tke budget are plotted against depth. In each plot the dissipation (thick black) is calculated as the residual of terms in (10). As a verification that the LES is resolving the relevant physics the SGS Reynolds stress contribution to the tke production from the mean shear (thick green) and Stokes shear (thick blue), and the Reynolds stress contribution to the pressure working transport term (thin black) are added to the resolved quantities and plotted as dashed lines. All the simulations that have enhanced turbulence by C-L wave forcing do a better job than the pure shear flow in closing the tke budget

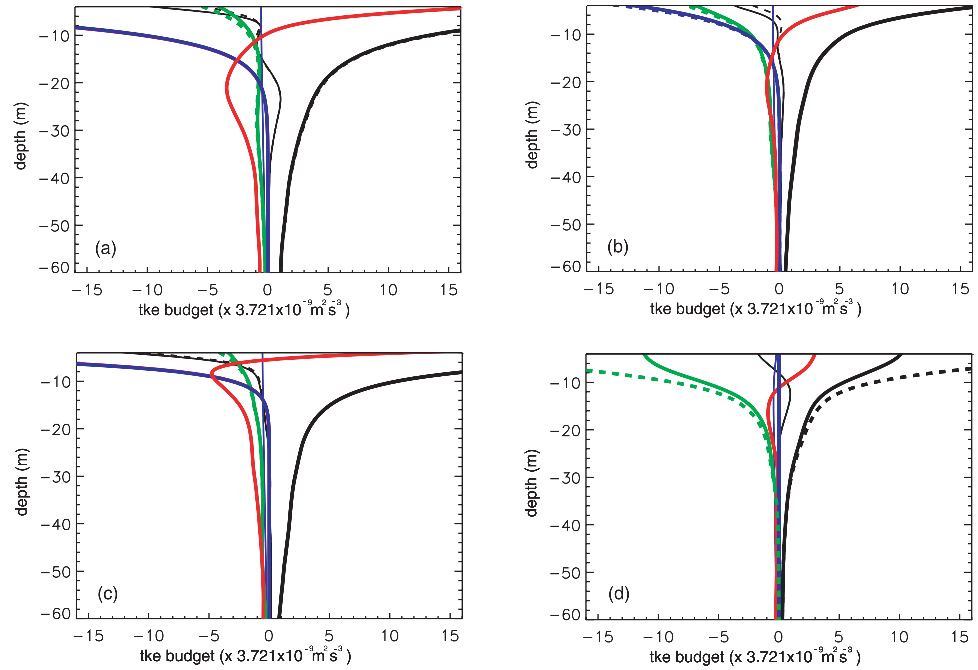

Figure 4. Turbulent kinetic energy budgets for selected simulations. (a) Control run R0. (b) R9; La_t is twice that in R0. (c) R15; k is twice that in R0. (d) R20; $La_t = \infty$. Thick green line, mean shear tke production; thick blue line, Stokes shear tke production; thick red line, vertical flux of tke. Thin black line, pressure working transport of tke; thin blue line, buoyancy production of tke; thick black line, dissipation. Dashed lines represent resolved plus SGS components of tke. Solid lines denote only the resolved components. The x axis is nondimensionalized with $v_*^3/\delta_e = 3.7 \times 10^{-9}$ m^2 s^{-3}.

without recourse to SGS processes. Grid resolution difficulties associated with ever decreasing eddy scales near a wall in a shear-driven boundary layer led to the stochastic backscatter boundary method [*Mason and Thompson*, 1992] but this is not necessary for our wave forced simulations as these budgets gives us confidence that SGS processes are not dominant in the wave forced energy budgets.

[24] Classically, in the absence of waves and buoyancy forcing, the production of tke is by the mean shear and is locally balanced by dissipation [*Wyngaard and Coté*, 1971]. This scenario is modeled in Figure 4d. With the C-L wave filtered equations there are two additional terms associated with the wave forcing, (as well as a modified pressure working term). Near the surface there is an additional source of tke (thick blue) where energy is extracted from the Stokes shear (that is, energy is extracted from the prescribed wave field by the resolved eddies). This production term partially balances the tke dissipation and, comparing the top panels, increases with U_s. There is also an additional vertical flux of tke (thick red) which acts to transport tke from the shallow tke production region (depths less than $2 \times \delta_s$) well into the mixed layer, where it balances the dissipation. Changing k, and hence δ_s (Figures 4a and 4c), changes the depth to which Stokes shear produces tke (thick blue) but also changes the depth at which the downward flux is greatest (that is when the vertical flux gradient of tke is zero). It happens that the vertical flux of tke is greatest at a depth of around $z = 2\delta_s$ (in accordance with the finding in the previous section where the downwelling intensity was maximal at two to three times the Stokes depth).

[25] In summary, the shear driven boundary layer has a localized tke balance between mean shear production of tke and dissipation. With waves effects tke production can be dominated by a Stokes shear production term that increases with the Stokes drift. Also with wave effects dissipation non locally balances production. Here a transport term closes the budget fluxing tke to a depth that depends on the Stokes depth scale.

4. Diagnosing the Occurrence of Langmuir Turbulence

[26] In this section we first look at bulk quantities to devise a way to characterize the turbulent flow. In particular we are interested in a diagnostic that contains depth varying information since we have already shown the depth structure to be dependent on the surface wave properties. We then investigate what external conditions result in Langmuir turbulence.

[27] Mean velocity and velocity variance plots (Figure 5) can be used to compare simulations with and without wave forcing (top and bottom plots, respectively). With waves the mean shear in the streamwise direction is greatly reduced consistent with enhanced mixing by streamwise Langmuir rolls. Considering the variance profiles in Figures 5b and 5d we see that without wave forcing $\overline{u'^2} > \overline{v'^2} > \overline{w'^2}$ and the turbulent dynamics are governed by shear generated in the streamwise direction by the wind stress. However, when the wave forcing is included there is a change in the order of the magnitudes of velocity variances and away from the

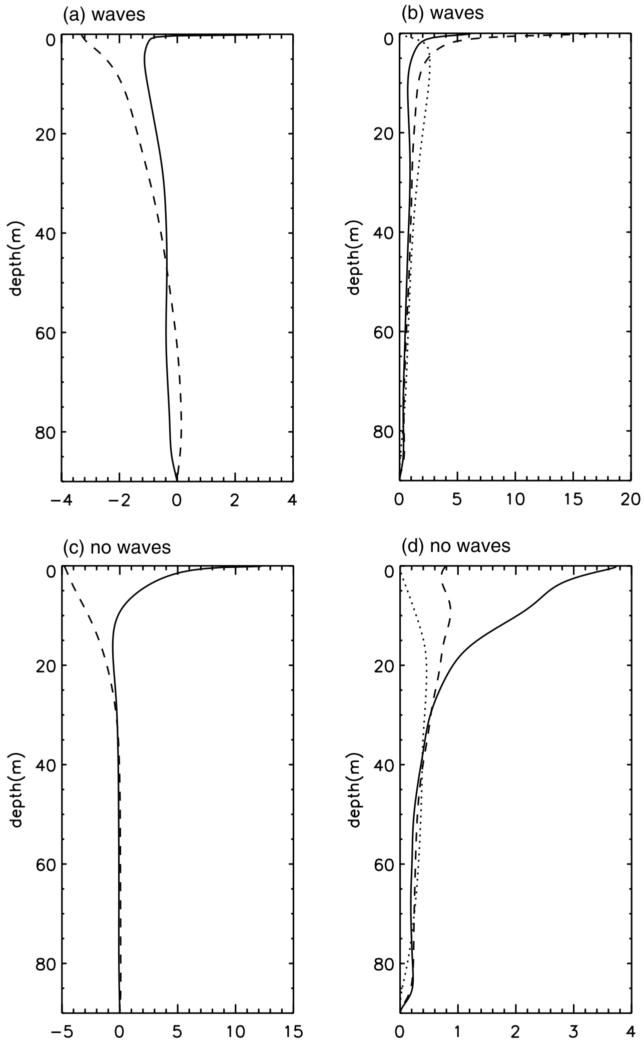

Figure 5. Nondimensional velocity profile statistics for (top) a simulation with wave forcing (R0) and (bottom) a simulation without wave forcing (R20). (left) Horizontal mean currents in the windward direction, $\overline{u}/v_*$ (solid line), and across wind direction, $\overline{v}/v_*$ (dashed line). (right) Resolved velocity variance profiles: $\overline{u'^2}/v_*^2$ (solid line), $\overline{v'^2}/v_*^2$ (dashed line), $\overline{w'^2}/v_*^2$ (dotted line).

surface $\overline{w'^2} > \overline{v'^2} > \overline{u'^2}$. Here pumping and across stream variance dominate the along stream variance consistent with the presence of streamwise aligned vortices, or more specifically, Langmuir rolls. Thus the variance plots show $\overline{w'^2} > \overline{v'^2} > \overline{u'^2}$ for Langmuir turbulence and $\overline{u'^2} > \overline{v'^2} > \overline{w'^2}$ for shear turbulence [*Teixeira and Belcher*, 2002].

[28] In order to investigate the depth dependence of the turbulent structure on La_t, using a single variable, we adopt the turbulent ratio, $R_t = \overline{w'^2}/(\overline{u'^2} + \overline{v'^2})$. In isotropic turbulence $R_t = 0.5$ since all the variances are identical. In shear driven turbulence R_t will increase with depth from $R_t = 0$ at the wall, where $w = 0$, until the turbulence is isotropic and $R_t = 0.5$. With Langmuir turbulence R_t will have a maximum between the surface and some deep isotropic depth. The shape of this profile characterizes the anisotropy in the Langmuir rolls. For example a shallow maximum would characterize turbulence from surface intensified downwelling jets.

[29] During the tke analysis the relative importance of mean shear production to Stokes shear production was highlighted. This observation motivates our choice of three simple diagnostics: R_t, $\partial|\boldsymbol{u}|/\partial z$ and $\partial u_s/\partial z$. Each of these vary with depth and are plotted for a number of simulations in Figure 6. Only the upper 30 m are plotted since below this depth the R_t quotient is not useful as the variances are so small (see Figure 5). The top left panel in Figure 6 shows a smoothly growing R_t profile (solid line) with depth. With $La_t = 0.6$ this simulation is in the transition part of phase space near the shear turbulence regime [*Li et al.*, 2005]. Decreasing La_t (moving across the panels) a turning point in R_t becomes more apparent as the Langmuir jets become relatively stronger. Notice also, decreasing δ_s (moving down the Figure 6 plots) results in shallower turning points in R_t as the depth of the wave forcing, and Langmuir turbulence, becomes surface intensified. These changes in the R_t profiles can be attributed to the changes in the Stokes and mean shear. Figure 6 also shows the profile of both the mean shear (dash-dotted line) and the Stokes shear (dashed line). These are both plotted on a logarithmic x axis so that the exponential Stokes shear is a straight line with surface intercept at U_s/δ_s and gradient $1/\delta_s$. Notice that increasing La_t corresponds to increasing the strength of the Stokes shear (dashed line) relative to the mean shear (dash-dotted line) and that decreasing δ_s decreases the depth at which the Stokes shear exceeds the mean shear. The depth of the turning point in R_t varies with the depth at which the Stokes shear dominates the mean shear. The magnitude of the R_t snout qualitatively varies with the magnitude of the Stokes shear.

[30] In summary, we see that Langmuir turbulence is dominant over shear turbulence when the Stokes shear exceeds the mean shear. This is because Langmuir turbulence is characterized by tke production from the Stokes shear rather than the mean shear. We see that the Stokes shear can dominate the mean shear either if La_t is sufficiently small or if δ_s is sufficiently small that the Stokes shear near the surface is sufficiently enhanced.

5. Discussion

[31] Using an ensemble of LES in a simplified scenario of the ocean mixed layer with parallel wind and an imposed wave forcing we have shown that Langmuir rolls form with properties that depend on La_t, δ_s and δ_e. The Langmuir rolls are explored by considering trajectories, instantaneous horizontal and vertical cross sections of vertical velocity and statistically steady turbulent kinetic energy budgets. We see evidence of episodic downwelling jets in the trajectory and instantaneous vertical velocity sections.

[32] Analysis of the tke budgets show the classic shear driven boundary layer has a localized tke balance between mean shear production of tke and dissipation. With the inclusion of waves effects tke production can be dominated by a Stokes shear production term that increases with the size of the Stokes drift term. Also with the inclusion of wave effects dissipation nonlocally balances production. In this scenario a vertical transport of tke is necessary to close the tke balance between near surface Stokes shear produc-

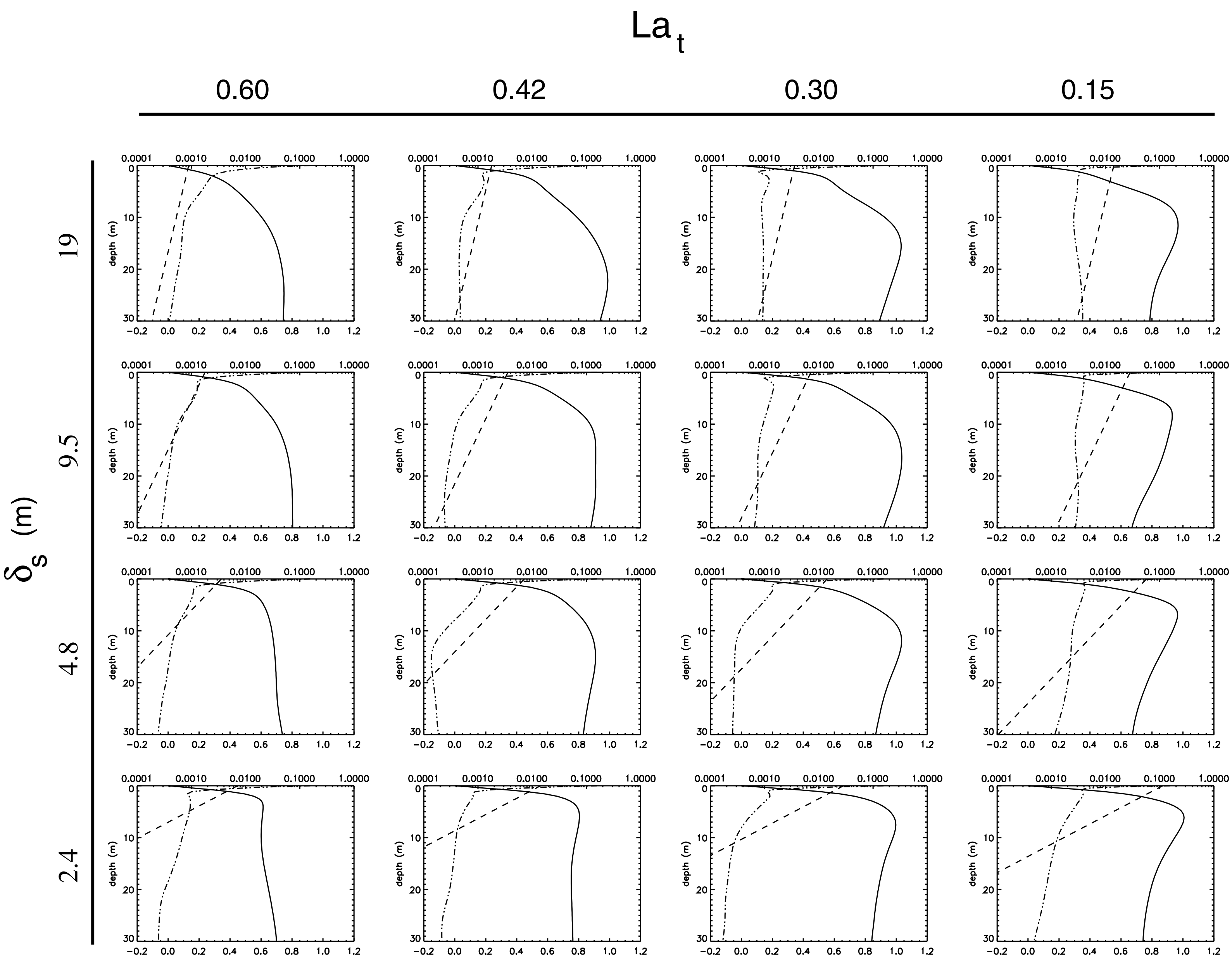

Figure 6. Shear and R_t profiles for simulations (top left) R1 to (bottom right) R16 presented on a grid as a function of δ_s and La_t. The solid line, $R_t = \overline{w'^2}/\overline{(u'^2 + v'^2)}$, is plotted on the lower x axis with range $[-0.2, 1.2]$. The dash-dotted line, $(\partial u/\partial z, \partial v/\partial z)$, is the mean shear and is plotted against values on the upper x axis logscale. The dashed line is the Stokes shear, $\partial u_s/\partial z$, also plotted against the upper x axis.

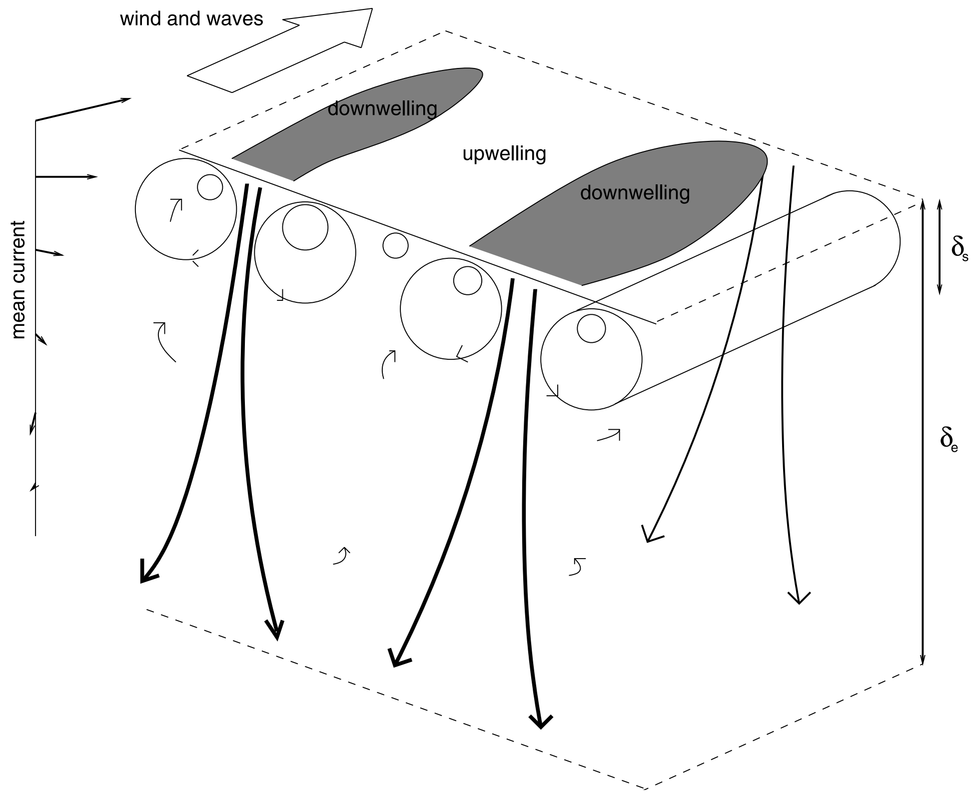

Figure 7. Illustration showing that when the wind and waves are aligned and the production from Stokes Shear dominates that from the mean shear, then downwelling jets inject fluid to the Ekman depth, which is typically greater than the depth of wave influence, δ_s.

tion and a more vertically distributed dissipation. The depth of maximum vertical flux of tke varies as a multiple of the Stokes depth scale.

[33] We construct a ratio R_t of the vertical to horizontal velocity variances as a diagnostic to quantify whether the turbulence is Langmuir-like or shear-like. Then, following our observations about the mean and Stokes shear production terms in the tke budgets we use R_t to show that Langmuir turbulence is dominant over shear turbulence when the Stokes shear exceeds the mean shear. This is because Langmuir turbulence is characterized by a tke production by the Stokes shear rather than the mean shear. We show that the Stokes shear can dominate the mean shear if La_t is sufficiently small [*Li et al.*, 2005] or if δ_s is sufficiently small such that the Stokes shear near the surface, which scales as U_s/δ_s, is enhanced.

[34] The wave-filtered Craik-Leibovich equations include two additional forcing terms in the momentum equations. Firstly, there is the Coriolis-Stokes forcing, $\boldsymbol{f} \times \boldsymbol{u_s}$, which acts as an effective boundary condition that rotates the net surface stress away from the along wind direction. This reduces the shear in the along stream direction, preconditioning the flow to the formation of along stream vortices [*Polton et al.*, 2005]. Secondly there is an additional vortex force term, $\boldsymbol{u_s} \times \boldsymbol{\omega}$, which is responsible for the formation of along stream Langmuir cell instabilities [*Leibovich*, 1983] by accelerating across stream surface flow perturbations into convergence zones. In conjunction, these two effects result in a reduced mean shear and enhanced vertical transport of tke into the mixed layer. We have shown here that these jets penetrate to depths greater than the anticipated depth scale for wave processes, the Stokes depth, instead being arrested at the Ekman depth scale (for $\delta_e > \delta_s$, as is typical in the ocean) and are represented schematically in Figure 7. In practice the base of the mixed layer is often shallower than the Ekman depth scale, in which case it seems probable that the vertical jets will enhance mixed layer deepening processes [*Li and Garrett*, 1997].

[35] Classically Langmuir circulations are though of as stream-wise counterrotating vortex rolls but it is important to emphasize the importance of these intense downwelling jets (Figure 7). It is these jets which will control episodic deepening of the mixed layer, rapid penetration and mixing of tracers and could also dissipate energy via the generation and propagation of internal waves.

[36] **Acknowledgments.** The research presented in this paper was funded by the Leverhulme Trust under grant F/00239/A and the US Office of Naval Research under grant N-00014-01-1-0133. We thank the two anonymous reviewers for their useful comments and suggestions.

References

Blackadar, A. K. (1962), The vertical distribution of wind and turbulent exchange in a neutral atmosphere, *J. Geophys. Res.*, *67*, 3095–3102.

Brown, A. R., J. M. Hobson, and N. Wood (2001), Large-eddy simulation of neutral turbulent flow over rough sinusoidal ridges, *Boundary Layer Meteorol.*, *98*, 411–441.

Coleman, G. N. (1999), Similarity statistics from a direct numerical simulation of the neutrally stratified planetary boundary layer, *J. Atmos. Sci.*, *56*, 891–900.

Craig, P. D., and M. L. Banner (1994), Modeling wave-enhanced turbulence in the ocean surface layer, *J. Phys. Oceanogr.*, *24*, 2546–2559.

Craik, A. D. D., and S. Leibovich (1976), A rational model for Langmuir circulations, *J. Fluid Mech.*, *73*, 401–426.

Gargett, A. E., J. Wells, A. E. Tejada-Martinez, and G. E. Grosch (2004), Langmuir supercells: a mechanism for sediment resuspension and transport in shallow seas, *Science*, *306*, 1925–1928.

Gnanadesikan, A., and R. A. Weller (1995), Structure and instability of the Ekman spiral in the presence of surface gravity waves, *J. Phys. Oceanogr.*, *25*, 3148–3171.

Holm, D. D. (1996), The ideal Craik-Leibovich equations, *Physica D*, *98*, 415–441.

Langmuir, I. (1938), Surface motion of water induced by wind, *Science*, *87*, 119–123.

Leibovich, S. (1983), The form and dynamics of Langmuir circulations, *Annu. Rev. Fluid Mech.*, *15*, 391–427.

Lewis, D. M. (2005), A simple model of plankton population dynamics coupled with a LES of the surface mixed layer, *J. Theor. Biol.*, *234*, 565–591.

Lewis, D. M., and S. E. Belcher (2004), Time-dependent, coupled, Ekman boundary layer solutions incorporating Stokes drift, *Dyn. Atmos. Oceans*, *37*, 313–351.

Li, M., and C. Garrett (1997), Mixed layer deepening due to Langmuir circulation, *J. Phys. Oceanogr.*, *27*, 121–132.

Li, M., C. Garrett, and E. Skyllingstad (2005), A regime diagram for classifying turbulent large eddies in the upper ocean, *Deep Sea Res., Part I*, *52*, 259–278.

Mason, P. J., and R. I. Sykes (1982), A two-dimensional numerical study of horizontal roll vortices in an inversion capped planetary boundary layer, *Q. J. R. Meteorol. Soc.*, *108*, 801–823.

Mason, P. J., and D. J. Thompson (1992), Stochastic backscatter in large-eddy simulations of boundary layers, *J. Fluid Mech.*, *242*, 51–78.

McWilliams, J. C., P. P. Sullivan, and C.-H. Moeng (1997), Langmuir turbulence in the ocean, *J. Fluid Mech.*, *334*, 1–30.

Noh, Y., H. S. Min, and S. Raasch (2004), Large eddy simulation of the ocean mixed layer: The effects of wave breaking and Langmuir circulation, *J. Phys. Oceanogr.*, *34*, 720–735.

Phillips, O. M. (1977), *Dynamics of the Upper Ocean*, 336 pp., Cambridge Univ. Press, New York.

Plueddemann, A. J., J. A. Smith, D. M. Farmer, R. A. Weller, W. R. Crawford, R. Pinkel, S. Vagle, and A. Gnanadesikan (1996), Structure and variability of Langmuir circulation during the surface waves processes program, *J. Geophys. Res.*, *101*, 3525–3543.

Pollard, R. T., and K. J. H. Thomas (1989), Vertical circulation revealed by diurnal heating of the upper ocean in late winter: Part I: Observations, *J. Phys. Oceanogr.*, *19*, 269–278.

Polonichko, V. (1997), Generation of Langmuir circulation for nonaligned wind stress and the stokes drift, *J. Geophys. Res.*, *102*, 15,773–15,780.

Polton, J. A., D. M. Lewis, and S. E. Belcher (2005), The role of wave-induced Coriolis-Stokes forcing on the wind-driven mixed layer, *J. Phys. Oceanogr.*, *35*, 444–457.

Skyllingstad, E. D., and D. W. Denbo (1995), An ocean large-eddy simulation of Langmuir circulations and convection in the surface mixed layer, *J. Geophys. Res.*, *100*, 8501–8522.

Skyllingstad, E. D., W. D. Smyth, and G. B. Crawford (2000), Resonant wind-driven mixing in the ocean boundary layer, *J. Phys. Oceanogr.*, *30*, 1866–1890.

Smagorinsky, J. (1963), General circulation experiments with the primitive equations, I: The basic experiment, *Mon. Weather Rev.*, *91*, 99–164.

Smyth, W. D., E. D. Skyllingstad, G. B. Crawford, and H. Wijesekera (2002), Nonlocal fluxes and Stokes drift effects in the K-profile parameterization, *Ocean Dyn.*, *52*, 104–115.

Sullivan, P. P., J. C. McWilliams, and W. K. Melville (2004), The oceanic boundary layer driven by wave breaking with stochastic variability. I: Direct numerical simulations, *J. Fluid Mech.*, *507*, 143–174.

Teixeira, M. A. C., and S. E. Belcher (2002), On the distortion of turbulence by a progressive surface wave, *J. Fluid Mech.*, *458*, 229–267.

Thorpe, S. A. (2004), Langmuir circulation, *Annu. Rev. Fluid Mech.*, *36*, 55–79.

Wood, N., and P. Mason (1993), The pressure force induced by neutral, turbulent flow over hills, *Q. J. R. Meteorol. Soc.*, *119*, 1233–1267.

Wood, N., F. Hewer, and M. Hobson (1998), *BLASIUS Version 3.03: Documentation of a Model of Flow over Hills*, 71 pp., UK Met Office, Reading, U. K.

Wyngaard, J. C., and O. R. Coté (1971), The budgets of turbulent kinetic energy and temperature variance in the atmospheric surface layer, *J. Atmos. Sci.*, *28*, 190–201.

Zikanov, O., D. N. Slinn, and M. R. Dhanak (2003), Large-eddy simlations of the wind-induced turbulent Ekman layer, *J. Fluid Mech.*, *495*, 343–368.

S. E. Belcher, Department of Meteorology, University of Reading, P.O. Box 243, Reading, Berkshire, RG6 6BB, UK. (s.e.belcher@reading.ac.uk)

J. A. Polton, Scripps Institution of Oceanography, University of California, San Diego, 9500 Gilman Drive, La Jolla, CA 92093-0213, USA. (jpolton@ucsd.edu)